JOURNAL OF THE AMERICAN CHEMICAL SOCIETY
pubs.acs.org/JACS
Article

High-Performance Iridium–Molybdenum Oxide Electrocatalysts for Water Oxidation in Acid: Bayesian Optimization Discovery and Experimental Testing

Jacques A. Esterhuizen,[§] Aarti Mathur,[§] Bryan R. Goldsmith, and Suljo Linic*

Cite This: *J. Am. Chem. Soc.* 2024, 146, 5511–5522
Read Online

ABSTRACT: Ir oxides are costly and scarce catalysts for oxygen evolution reaction (OER) in acid. There has been extensive interest in developing alternatives that are either Ir-free or require smaller amounts of Ir to drive the reactions at acceptable rates. One design strategy is to identify Ir-based mixed oxides that achieve similar performance while requiring smaller amounts of Ir. The obstacle to this strategy has been a very large phase space of the Ir-based mixed metal oxides, in terms of the metals combined with Ir and the different crystallographic structures of the mixed oxides, which prevents a thorough exploration of possible materials. In this work, we developed a workflow that uses machine-learning-aided Bayesian optimization in combination with density functional theory to make the exploration of this phase space plausible. This screening identified Mo as a promising dopant for forming acid-tolerant Ir-based oxides for the OER. We synthesized and characterized the Ir–Mo mixed oxides in the form of thin-film electrocatalysts with a known surface area. We show that these mixed oxides exhibited overpotentials ~30 mV lower than a pure Ir control while maintaining 24% lower Ir dissolution rates than the Ir control. These findings suggest that Mo is a promising dopant and highlight the promise of machine learning to guide the experimental exploration and optimization of catalytic materials.

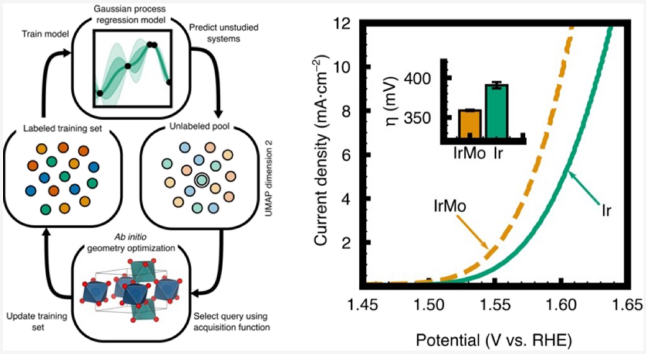

■ INTRODUCTION

Electrochemical water splitting is a promising carbon-free avenue for hydrogen generation.[1] Currently, proton-exchange membrane (PEM) electrolyzers that operate in acidic electrolytes exhibit superior performance to alkaline anion-exchange membrane electrolyzers across numerous metrics, including higher voltage efficiencies, gas purities, current densities, partial load efficiencies, as well as compact system design and faster power responses.[2] Despite these advantages, the widespread use of PEM electrolyzers has been prevented due to a lack of suitable electrocatalysts for the acidic oxygen evolution reaction (OER).[2−4]

The only PEM-compatible solid OER catalysts are Ru- and Ir-based oxides.[5,6] While Ir- and Ru-based electrocatalysts show promise, their widespread deployment is hindered by high cost, scarcity, underdeveloped supply chains, and limited activity and stability under OER conditions. A promising strategy to reduce costly Ir or Ru metal loadings is to form mixed or doped Ir- and Ru-based oxides.[2,7−12] Although these strategies have yielded mixed oxides that show improved initial electrocatalytic OER activity, their stability is at best similar and often lower than the stability of the respective pure metal materials.[13] For example, dissolution measurements have shown that many mixed oxide catalysts containing Ir or Ru undergo significant and rapid leaching, leaving behind amorphous IrO_x or RuO_x active phases.[8−10,14,15]

The main challenge in identifying novel OER electrocatalysts is that it is a multiobjective optimization problem, where the designed materials should exhibit improvements, relative to the current state-of-the-art, in several attributes with design trade-offs between catalyst cost, stability, and activity.[16] A large number of optimization variables along with the huge phase space of potential mixed oxide materials, in terms of their compositions and their crystallographic structure, make the search for new mixed oxide materials challenging. Herein, we developed a machine learning (ML)-augmented density functional theory (DFT) modeling framework to screen for promising mixed Ir oxide OER electrocatalysts. We focused on $Ir_{0.5}M_{0.5}O_x$ compositions, where M is an additive metal and M = Ti, V, Cr, Mn, Fe, Co, Ni, Cu, Zr, Nb, Mo, Ru, Rh, Pd, Ag, Hf, Ta, W, Re, Os, Ir, Pt, and Au. Our ML approach focuses on

Received: November 30, 2023
Revised: January 29, 2024
Accepted: February 5, 2024
Published: February 19, 2024

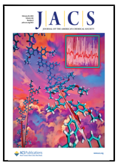

https://doi.org/10.1021/jacs.3c13491
J. Am. Chem. Soc. 2024, 146, 5511–5522

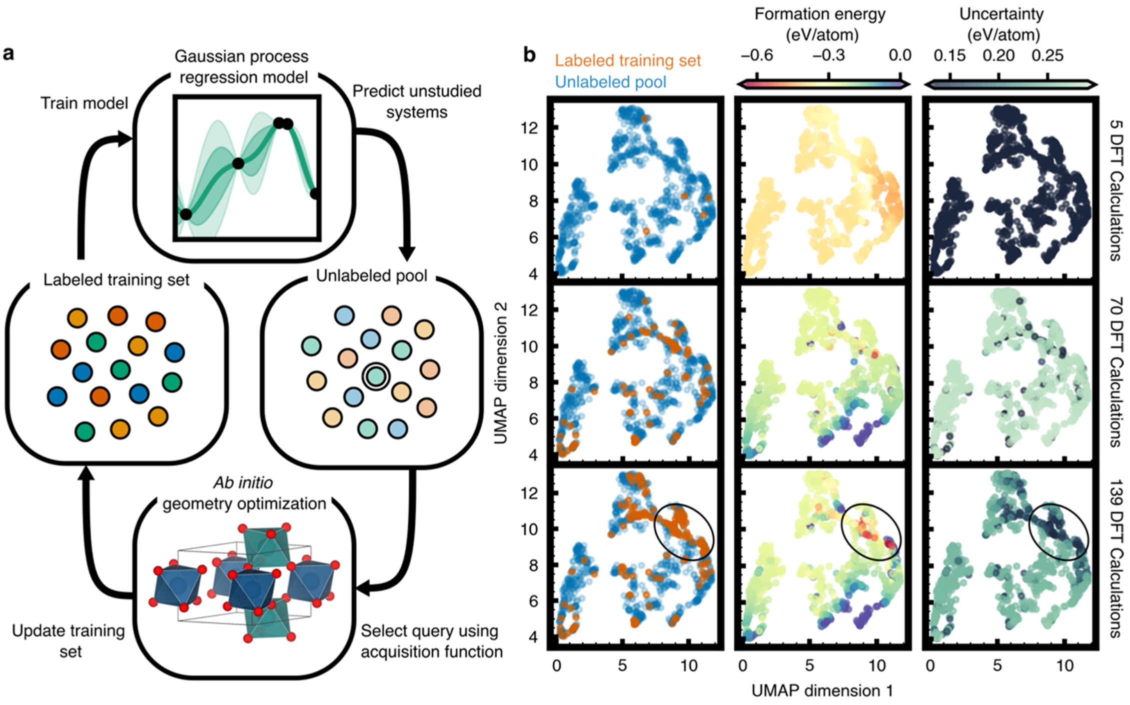

Figure 1. Bayesian global optimization (BO) for $Ir_{0.5}M_{0.5}O_x$. (a) Schematic depiction of the BO workflow. We train a Gaussian process regression model on an initial sparse labeled training set and then use it to predict the energies of the remaining unstudied materials. We query one of the unstudied (unlabeled) structures for DFT geometry optimization using the expected improvement acquisition function and then update the training set. We continue this process iteratively until we reach convergence criteria. (b) Illustrative progression of the BO workflow from initialization (5 DFT-studied structures) to convergence (139 DFT-studied structures) for $Ir_{0.5}Mo_{0.5}O_2$. The far-left panels show the points we have studied with DFT (labeled training set) and the points that we are predicting with Gaussian process regression (unlabeled pool); the middle panel shows the formation energies predicted by Gaussian process regression, and the far-right panel shows the uncertainties of the Gaussian process regression predictions. The circled region encloses the identified materials with a low formation energy and high model certainty.

the mixed oxide stability at the electrochemically relevant acidic OER potentials and pHs as the critical figure or merit since this is an essential requirement for a viable electrocatalyst. The screening approach is based on using ML-aided Bayesian optimization (BO), which allowed us to dramatically reduce the number of DFT calculations required to identify the most promising (stable) $Ir_{0.5}M_{0.5}O_x$ materials.

Based on the screening, we identified Mo-doped IrOx ($Ir_{0.5}Mo_{0.5}O_x$) as a promising electrocatalyst. To test the predictions of the screening, we synthesized and characterized $Ir_{0.5}Mo_{0.5}O_x$ electrocatalysts in the form of thin mixed oxide films on heavily doped conducting Si substrates. Rigorous electrochemical testing demonstrated that the Mo-doped Ir oxide exhibited overpotentials that are ∼30 mV lower than pure IrO_x per identical electrocatalyst surface areas while maintaining lower Ir dissolution rates compared to the IrO_x control. In addition to ($Ir_{0.5}Mo_{0.5}O_x$), our ML-enabled Bayesian screening framework also identified several other promising mixed Ir oxides, which had been previously studied, giving additional confidence in the overall approach. The contribution represents a comprehensive approach that combines atomistic modeling of the material stability with ML and Bayesian optimization to rapidly identify novel mixed oxide compositions for OER electrocatalysis.

■ RESULTS

Bayesian Optimization to Screening for Electrochemically Stabile Mixed Oxides. We used a BO algorithm combined with DFT modeling, schematically shown in Figure 1a, to identify electrochemically stable $Ir_{0.5}M_{0.5}O_2$ and $Ir_{0.5}M_{0.5}O_3$ model structures.[17] BO algorithms have been used previously to accelerate the discovery of small inorganic molecules, nanoporous materials, and catalysts.[18−21] The central idea of the BO algorithm is to optimize a computationally expedient surrogate model instead of an expensive function. In our case, the surrogate model is a Gaussian process (GP) regressor[22] and the expensive function evaluation is a DFT calculation of the ground-state energy of a material. The BO algorithm uses an acquisition function to take both the GP regressor prediction and uncertainty into account in order to decide which DFT calculations to perform. The acquisition function guides the sampling process in a quantitative manner such that exploitation (i.e., studying predicted low-energy DFT structures with respect to the observed data) and exploration (i.e., studying uncertain but higher-energy DFT structures with respect to the observed data that will improve the model) are balanced. We investigated several acquisition functions for our application, including expected improvement,[23] probability of improvement,[24] and Gaussian process lower confidence bound.[25] We found similar performance across all acquisition functions (Figure S1) and thus proceeded with the expected improvement acquisition function to determine which data points should be labeled by DFT calculations.[22,23] Further details on the BO workflow and details on the GP model training (e.g., choice of kernel and featurization scheme) are given in the Methods section.

We considered M = Ti, V, Cr, Mn, Fe, Co, Ni, Cu, Zr, Nb, Mo, Ru, Rh, Pd, Ag, Hf, Ta, W, Re, Ir, Pt, and Au as elements that can be combined with Ir to form mixed oxides. Geometries of the $Ir_{0.5}M_{0.5}O_2$ and $Ir_{0.5}M_{0.5}O_3$ data sets were

https://doi.org/10.1021/jacs.3c13491
J. Am. Chem. Soc. 2024, 146, 5511−5522

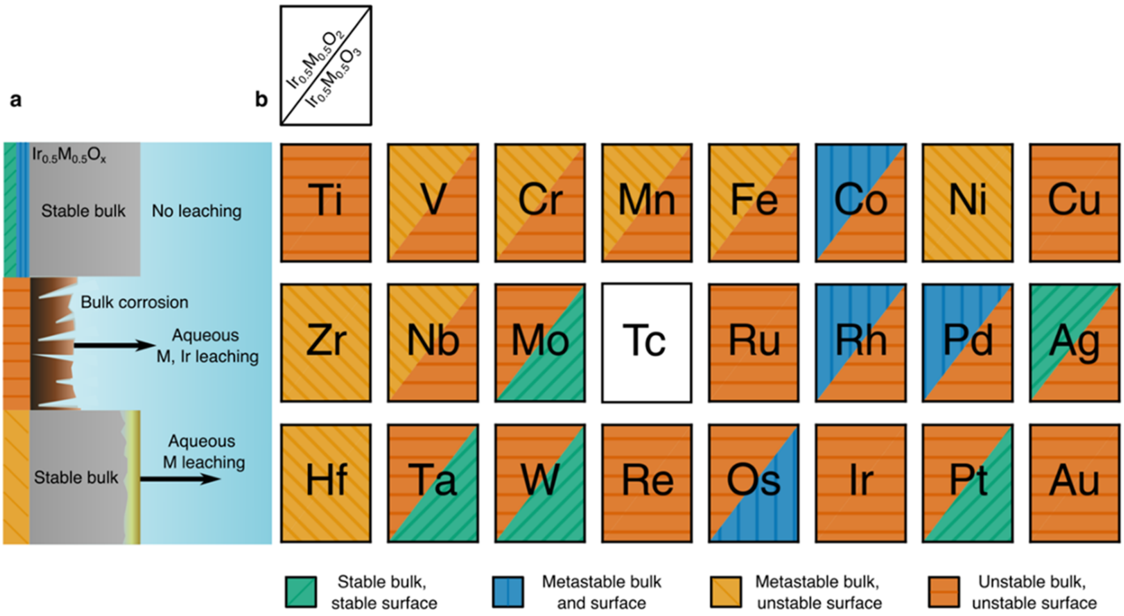

Figure 2. Bulk electrochemical stability of $Ir_{0.5}M_{0.5}O_x$. (a) Schematic showing an illustration of how a doped $Ir_{0.5}M_{0.5}O_x$ surface changes in each stability region. The main text contains additional information regarding the energetic criteria for materials falling into each stability category. (b) Map of the elements M considered as additives colored according to predicted electrochemical stability at 1.6 V vs SHE and pH = 1. Tc was not considered as an additive because of its radioactive nature. The upper half of each box denotes the predicted stability of the $Ir_{0.5}M_{0.5}O_2$ polymorphs, and the lower half denotes the predicted stability of the $Ir_{0.5}M_{0.5}O_3$ polymorphs.

obtained by querying all crystal structures with ABC_4 and ABC_6 stoichiometries, respectively, under the assumption that one of either the ABC_4 or ABC_6 crystal structures would be a representative model system for each Ir and dopant metal mixed oxide. To accomplish this task, we used the Materials Project database and performed point-wise replacement of the A- or B-site elements with either Ir or M and the C-site element with O, leading to solid-solution doped mixed Ir oxides.[26] This process led to 5,944 $Ir_{0.5}M_{0.5}O_2$ and 1660 $Ir_{0.5}M_{0.5}O_3$ materials (polymorphs) for each dopant metal M. Redundant systems were identified using a structure matching routine in Pymatgen and removed,[27] reducing the structure space to 1014 $Ir_{0.5}M_{0.5}O_2$ and 309 $Ir_{0.5}M_{0.5}O_3$ unique materials for each dopant metal M.

Our results suggest that the BO workflow effectively balances exploration and exploitation of the chemical space, as illustrated in Figure 1b, by a concrete example of identifying the lowest energy $Ir_{0.5}Mo_{0.5}O_2$ structures. Data in Figure 1b show the time evolution of the BO workflow, where we use the uniform manifold approximation and projection algorithm (UMAP),[28] a nonlinear dimensionality reduction method, to visualize the chemical space of structures studied and show the progress of the BO workflows over time. At the beginning of the workflow, when we have computed energies of only five structures with DFT, the model generally performs poorly. It predicts near-constant formation energies for all structures and is overconfident in its predictions (corroborated by the calibration curves in Figure S2).[22] This counterintuitive result of overconfident behavior when less data is seen by the model is likely due to the fact that both the predictions and the uncertainty are model-derived and the model simply has not seen enough data with five samples to predict either quantity with a suitable resolution yet. After ~70 structures were computed with DFT, the chemical space is well-sampled, and the region of the chemical space where many of the low-energy structures exist is identified but not yet heavily explored. At the workflow conclusion, after 139 DFT calculations, the region of chemical space containing more low-energy structures (highlighted in the circled area) has been sampled much more heavily than the high-energy regions, leading to lower uncertainty in the low-energy region. We emphasize that reaching convergence after studying only 139 of 1014 structures with DFT corresponds to an 87.7% reduction in the number of geometry optimizations compared to studying the entire space with DFT, resulting in a near order of magnitude speedup. The Supporting Information additionally shows the BO workflow's progress when finding stable $Ir_{0.5}Mo_{0.5}O_3$ structures (Figure S3).

The most stable $Ir_{0.5}M_{0.5}O_x$ materials, identified using the BO routine, were analyzed for their stability based on their DFT energies and experimentally available ion and aqueous species energies.[29−31] We focused on the OER-relevant conditions of an applied potential of 1.65 V vs SHE and a pH of 1 due to their proximity to the experimentally relevant OER operating conditions. We based our classification of the material stability, summarized in Figure 2a, on prior work from Singh et al.[30] Materials were classified into four groups based on their decomposition free energies. We classified materials on the convex hull (considering the aqueous Ir−M−O−H composition space) as having stable bulk structures and stable surfaces, materials less than 0.5 eV/atom above the convex hull with solid decomposition products as having metastable bulks and metastable surfaces, materials less than 0.5 eV/atom above the convex hull with an aqueous ion of the additive metal as a decomposition product as having metastable bulk and unstable surfaces, and materials >0.5 eV/atom above the convex hull or exhibiting bulk geometries, in which not all of the metal atoms are octahedrally coordinated (with coordination geometries identified using the CrystalNN class in Pymatgen[27,32]) as unstable overall. The cutoff of 0.5 eV/atom for metastability was based on comparing with experimental reports of 20 materials (including metal oxides) and experimental inves-

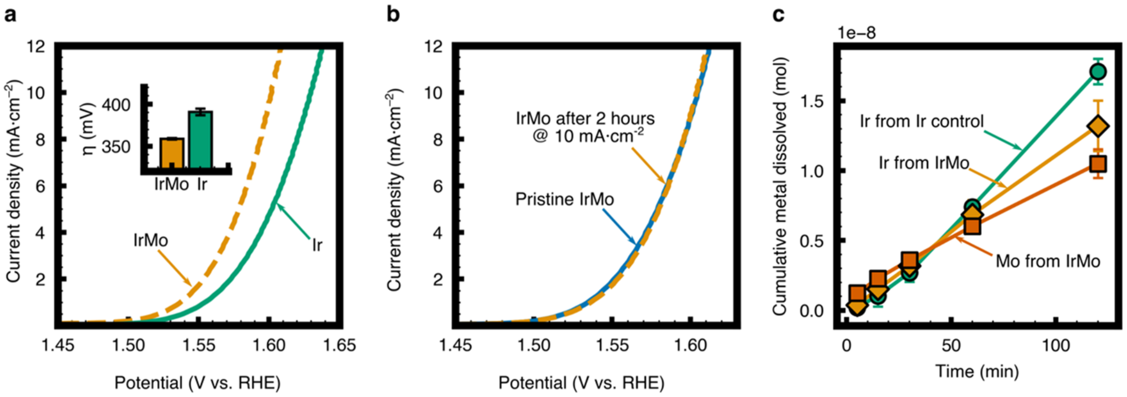

Figure 3. Experimental performance characterization of IrMo thin-film activity and stability by cyclic voltammetry and ICP-MS. (a) Representative current density versus voltage plot containing forward sweeps of Ir control and IrMo after electrochemical testing for 2 h. Shown in the inset are the average overpotentials at 10 mA·cm^{-2} over three independent samples, with the error bars representing the standard deviations over the samples. (b) Current density versus voltage plot of IrMo after low-current oxidative conditioning and after 2 h of steady-state testing through chronopotentiometry at 10 mA·cm^{-2}. (c) Amount of metal species present in electrolyte solution as a function of time for both the Ir control and IrMo. The error bars represent the standard deviations of the dissolution values over three independent samples.

tigations.[30] The accuracy of this thermodynamic metastability cutoff depends on the nature of the material decomposition products (e.g., solid phases, aqueous ions, solid phases, or a combination) and the energy barrier for decomposition. Manual inspection of structures not exhibiting full octahedral coordination of all metal atoms revealed the formation of molecular oxygen within the lattice of these structures, which we would expect to evolve and lead to structural rearrangement and bulk instability. Any material with two aqueous dissolution products would also be unstable, but this does not occur in this study, as Ir is always considered. Using these stability criteria, we classified all $Ir_{0.5}M_{0.5}O_x$ (x = 2 or 3) materials and found five stable mixed oxide materials, four materials with metastable bulk and metastable surfaces, 11 materials with metastable bulk and unstable surfaces, and 26 completely unstable materials. We summarize the results of our computational screening in Figure 2b.

The stability screening results in Figure 2b suggest several stable or metastable mixed oxide materials. The model predicts that under the relevant conditions, the $Ir_{0.5}M_{0.5}O_x$ materials containing additives of M = Co, Rh, Pd, or Os should form metastable Ir mixed oxides, while materials containing M = Mo, Ag, Ta, W, or Pt should be stable. Among the stable and metastable oxides, the 3d and early transition metals mixed with Ir are the most interesting due to their significantly reduced cost over platinum group metal additives. The $Ir_{0.5}M_{0.5}O_x$ catalysts, where M = Co, Ta, W, or Mo, exhibit a 50% reduction in platinum group metal content and have additive costs that are almost negligible compared to the Ir cost (Table S1).[33] We note that further reductions in catalyst cost are likely possible by exploring more Ir-dilute oxides or post-transition metal dopants that are earth-abundant and frequently stable in acidic solutions at OER-relevant potentials, but consideration of these is beyond the scope of this work.

Several mixed oxides identified in the BO screening as stable and potentially useful have exhibited promising OER activity and stability in prior experimental testing. For example, IrTa mixed oxides were recently shown to exhibit improved mass activities and turnover frequencies compared to an IrO_2 control, while a thorough stability analysis yielded comparable stability to rutile IrO_2 under acidic OER operating conditions.[34] Alloy nanoparticles of Rh and Ir exhibited mass activities higher than pure Ir nanoparticles toward OER in acid, with no apparent decreases in OER activity after 2000 cycles.[35] Ir−W nanodendrites exhibited turnover frequencies almost 2-fold higher than a pure Ir catalyst while exhibiting improved durability in extended electrochemical dissolution testing,[36] and mixed Ir and WO_3 catalysts exhibited high Ir mass activities while maintaining stable electrochemical performance in 0.5 M H_2SO_4.[12] We also find several additional mixed oxide materials that were not previously reported, such as $Ir_{0.5}Os_{0.5}O_x$ and $Ir_{0.5}Pt_{0.5}O_x$.

Another material of interest identified in our Bayesian ML screening that has not been thoroughly analyzed previously is Ir−Mo oxide. While the Bayesian optimization described above suggests that this material should be relatively stable, there are only a few conflicting reports on its activity and limited work characterizing the impact of Mo doping on Ir stability.[11,37−40] Due to the low cost of Mo and therefore a potential appeal of the mixed $Ir_{0.5}Mo_{0.5}O_x$ oxide, we rigorously experimentally investigated its performance in acidic OER.

Experimental Characterization of $Ir_{0.5}Mo_{0.5}O_x$ Stability and Activity. To test $Ir_{0.5}Mo_{0.5}O_x$ in acidic OER, we fabricated films of mixed Ir and Mo approximately 10 nm in total thickness by using direct current magnetron sputtering on degenerately doped p^+-Si. Degenerately doped p-type silicon or p^+-Si contains an abundance of holes for completing OER. We used a p^+-Si substrate to provide an atomically planar polished substrate for magnetron sputtering metal thin films. We refer to this sample as IrMo. We also fabricated a pure Ir film of 10 nm thickness on degenerately doped p^+-Si to use as a control in the OER measurements. The Methods section includes additional details regarding the synthesis methodology.

The IrMo and Ir samples were preoxidized electrochemically in a 10 min long chronopotentiometric hold at 1 mA·cm^{-2} in 0.5 M perchloric acid. The inductively coupled plasma mass spectrometry (ICP-MS) data in Figure S4 suggest that for both samples, no detectable amount of metal leaches into the solution within the conditioning period. The data in Figure S5 show that there is no obvious metal contamination in IrMo across a wide range of binding energies and near-equal atomic compositions of Ir and Mo. The data in Figures S6−S8 show X-ray photoelectron spectroscopy (XPS), demonstrating that the surface is oxidized after electrochemical conditioning.

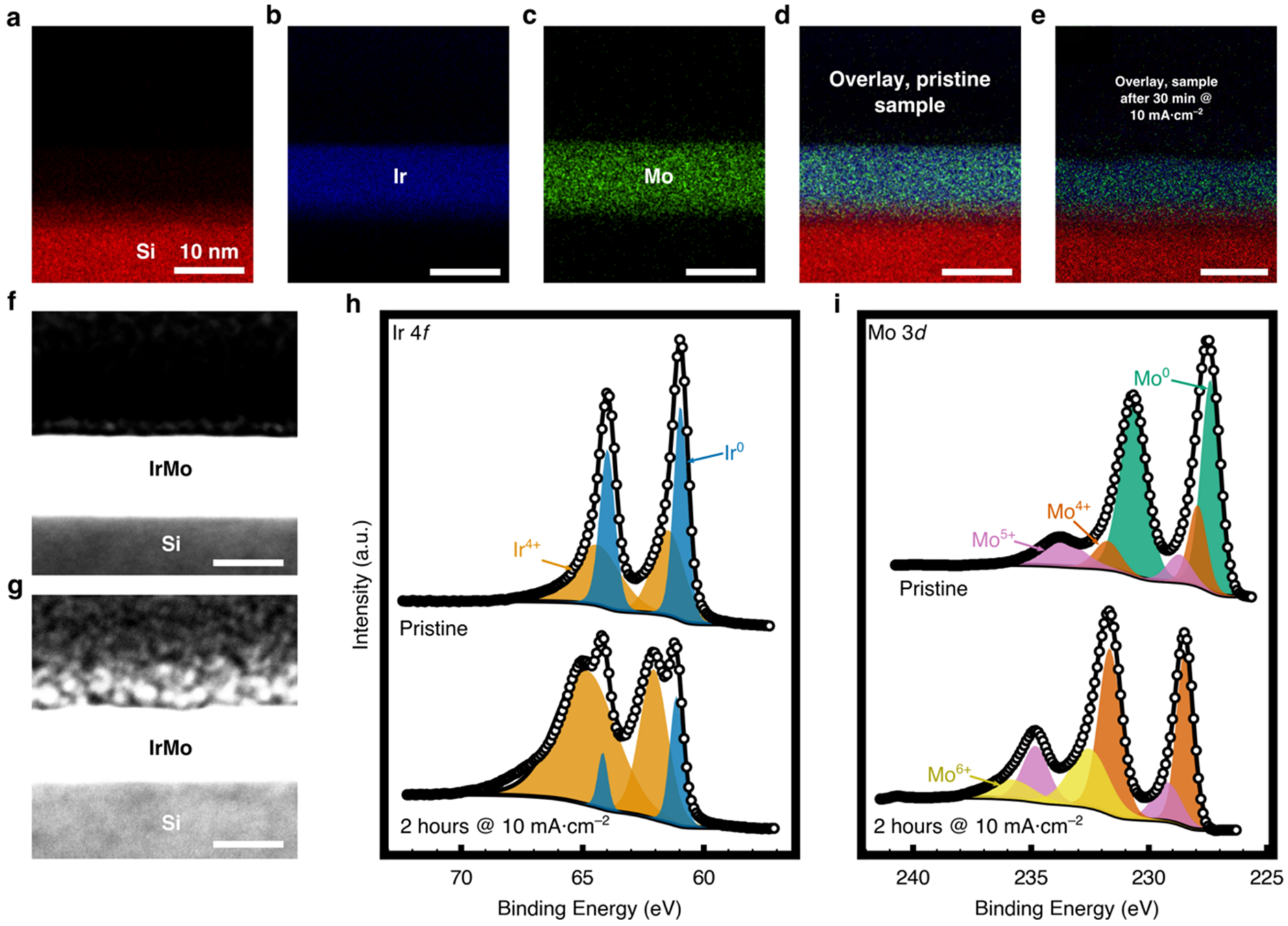

Figure 4. Micrographic and spectroscopic characterization of synthesized IrMo thin films. Energy-dispersive X-ray spectroscopy elemental mappings of (a) Si, (b) Ir, and (c) Mo for the pristine sample, and overlays of the three for both the (d) pristine and (e) tested (30 min of chronopotentiometry at 10 mA·cm^{-2}) IrMo samples. Dark-field TEM images of both the (d) pristine and (e) tested (30 min of chronopotentiometry at 10 mA·cm^{-2}) IrMo samples. All scale bars in panels (a−g) are 10 nm in size. XPS spectra of (h) Ir 4f and (i) Mo 3d are shown for the pristine samples and samples after 2 h of chronopotentiometry at 10 mA·cm^{-2}. The scattered points indicate the raw data, and the overall fitting envelope is indicated by a black line. For each oxidation state, color indicates the combined spin−orbit split components.

The electrocatalytic OER performance of the conditioned Ir and IrMo samples was tested in 0.5 M perchloric acid. We used cyclic voltammetry to determine the onset potentials defined as the potential at which a 10 mA·cm^{-2} current was achieved. The samples were scanned from ∼1.0 to 1.65 V vs RHE at a sweep rate of 100 mV·s^{-1}. The data in Figure 3a show the average resulting cyclic voltammograms upon repeating this electrochemical testing over three different samples. The average onset potential of the Ir sample was 1.621 ± 0.001 V vs RHE (corresponding to an overpotential of 391 mV), whereas the average onset potential of the IrMo sample was 1.589 ± 0.004 V vs RHE (corresponding to an overpotential of 359 mV). The measurements show an improvement of 32 ± 3 mV in measured overpotential for IrMo compared to Ir.

In addition to electrochemical activity measurements, the stability of both systems over time was studied by performing steady-state stress testing. In these chronopotentiometry measurements, following a standard protocol for the long-term stress testing of OER electrocatalysts, the electrocatalysts were held at 10 mA·cm^{-2} for an extended period of time.[5] Figure S9 shows the data for the chronopotentiometry scans. Data in Figure 3b show the overlay of the *I*−*V* performance of the IrMo electrocatalysts before and after two h of the chronopotentiometry testing. The data show that the CV curves are nearly identical for the fresh and tested samples, with an overlaid onset potential and CV slope. This performance stability indicates that the electrocatalytic activity of the IrMo samples does not degrade after 2 h of the steady-state operation. The cyclic voltammetry results for the IrMo sample largely mirror those for the Ir control sample (Figure S10), which also remains highly active after two h of testing.

The stress tests discussed above showed that the electrochemical performance of the two samples is stable. It must be noted, however, that this is not a sufficient indication of the inherent stability of the two electrocatalysts under OER conditions since it is in principle possible to maintain a high activity even if there is a degree of metal leaching into the electrolyte solution. We used ICP-MS to probe the dissolution behavior of the thin-film electrocatalysts during chronopotentiometric stress testing. Aliquots of electrolytes were taken 5, 15, 30, 60, and 120 min into the chronopotentiometry stress test experiment and evaluated for trace metal content using ICP-MS.

The data in Figure 3c show the amount of metal leached by both the Ir and IrMo samples over time. The data show that Ir is leaching from the Ir control sample at a higher rate

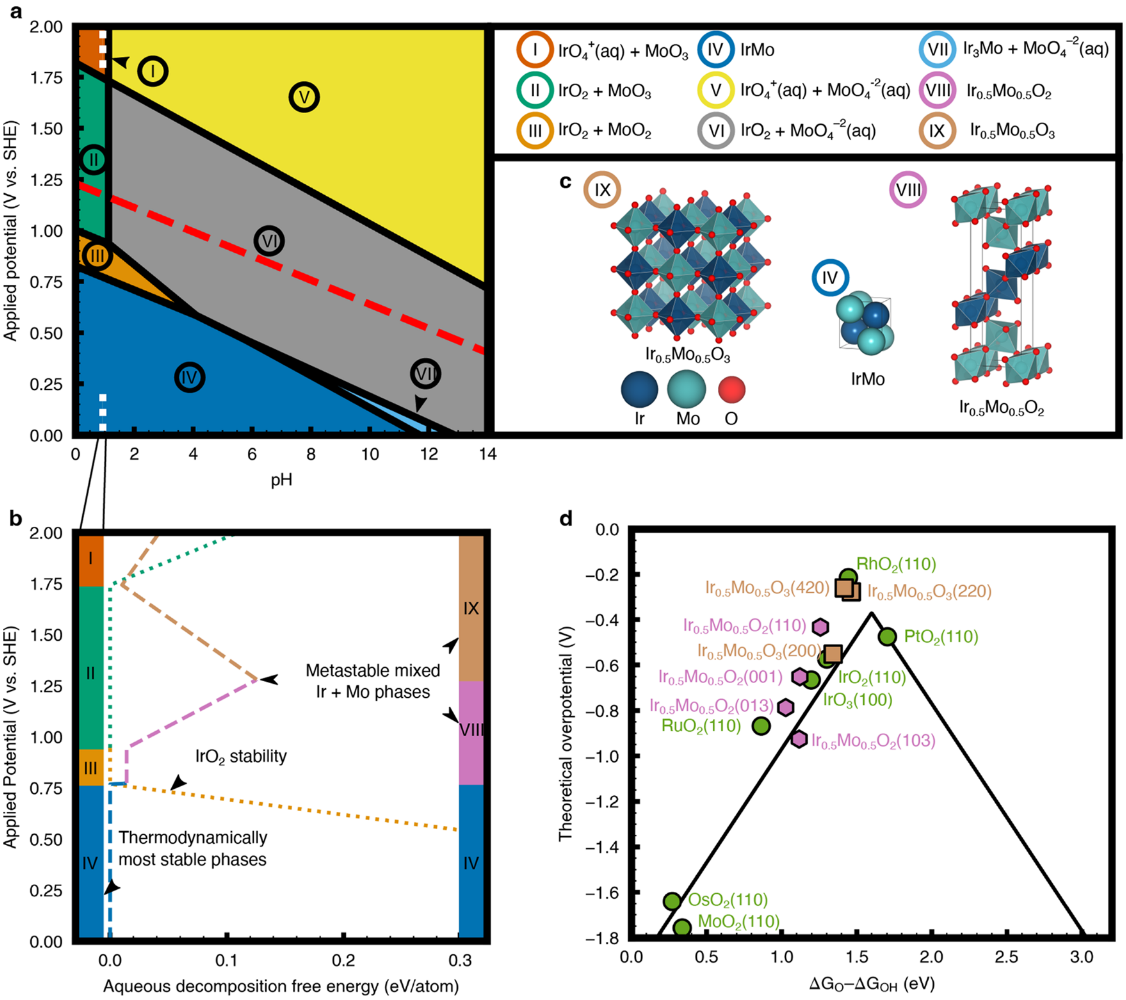

Figure 5. Computational characterization of $Ir_{0.5}Mo_{0.5}O_x$ stability and activity. (a) Bulk Pourbaix diagram showing the thermodynamically stable phases of the Ir−Mo−H_2O system as a function of pH and applied potential relative to the standard hydrogen electrode (SHE). The dashed red line indicates the equilibrium potential of the OER (1.23 vs RHE). We show all species used to construct the Pourbaix diagram in Table S3. (b) Calculated aqueous decomposition free energies of $Ir_{0.5}Mo_{0.5}O_x$ as a function of the applied potential at pH = 1. The dotted line shows the decomposition free energy of IrO_2 and the corresponding molybdenum oxide phase (MoO_2 or MoO_3 based on color), whereas the dashed line indicates the decomposition free energy of mixed Ir and Mo phases. The color panel on the left indicates the thermodynamically lowest-in-energy phase over each potential window. The color paneling on the right shows the lowest-in-energy mixed Ir and Mo phases over each potential window. (c) The bulk IrMo, $Ir_{0.5}Mo_{0.5}O_2$, and $Ir_{0.5}Mo_{0.5}O_3$ structures that correspond to the lowest-in-energy mixed Ir and Mo phases in (b). We identified these structures in our BO workflow. The $Ir_{0.5}Mo_{0.5}O_2$ structure is isomorphic to a $TiWO_4$ polymorph corresponding to Materials Project entry mp-753512, and the $Ir_{0.5}Mo_{0.5}O_3$ structure is isomorphic to a $NaSbF_6$ polymorph corresponding to Materials Project entry mp-1200829. (d) Calculated OER overpotentials of several $Ir_{0.5}M_{0.5}O_2$ and $Ir_{0.5}M_{0.5}O_3$ surfaces are shown as a function of the adsorption free energy difference between *O and *OH and compared to select pure oxides. The black line indicates the universal OER volcano, constructed using adsorbate linear scaling relationships and given by $\eta^{OER} = \max[(\Delta G_O - \Delta G_{OH}), 3.2\ \text{eV} - (\Delta G_O - \Delta G_{OH})]/e - 1.23$.[44] Further details regarding surface calculations are given in the Methods section.

compared to that of the IrMo samples. On the other hand, the total rate of metal (Ir + Mo) leaching from the IrMo sample is slightly higher than the leaching of Ir from the Ir control sample. It is important to note that the rate of leaching of Ir and Mo from the mixed alloy sample is similar to that of each other, so the composition of Ir and Mo in IrMo remains near the initial 50/50 throughout. The observation that the rate of Ir leaching in IrMo is lower than the rate of Ir leaching in the Ir sample is consequential since Ir is much more costly than Mo, and therefore, based on the materials' cost, it is in principle equally costly to synthesize twice as much of the IrMo catalysts relative to the Ir catalyst. If we account for the rate of Ir leaching and normalize this with respect to the cost of the electrocatalyst, the IrMo mixed oxide would last longer under these conditions. If we add to this the above-discussed fact the inherent IrMo activity is higher than the activity of Ir, the analysis suggests that the productivity of IrMo mixed oxide electrocatalysts, defined as an inherent reaction rate per Ir divided by the rate of leaching of Ir atoms, is significantly larger than the Ir electrocatalyst.

We also performed scanning transmission electron microscopy (STEM) and elemental analysis by energy-dispersive X-ray spectroscopy (EDX) on cross sections of the IrMo samples, as shown in Figure 4a−g. The cross-sectional images in Figure 4a−c show individual elemental scans of the Si, Ir, and Mo atoms in the preoxidized IrMo, and Figure 4d shows an overlay of the elemental scans from Figure 4a−c. The EDX results in Figure 4a−d show that the IrMo sample consists of a highly uniform planar film of well-mixed Ir and Mo of 11.6 nm thickness. Figure 4e shows an elemental overlay of the IrMo sample after 30 min of steady-state testing at 10 mA·cm^{-2}. The elemental mapping in Figure 4e suggests that Ir and Mo remain well-mixed throughout the film after steady-state testing. Images in Figure 4f,g show dark-field TEM scans of IrMo before and after 30 min of the steady-state testing, respectively. The micrographs suggest that the IrMo sample slightly roughens upon electrochemical testing, with small valleys appearing in the post-testing electron micrograph in Figure 4g. Nonetheless, these films appear to be smooth on atomistic scales with the surface maintaining a planar structure with no significant defects, as evidenced by a coarse-grained electron micrograph taken at the 50 nm scale, as shown in Figure S11.

We further characterized the $Ir_{0.5}Mo_{0.5}O_x$ thin-film electrocatalysts before and after testing using XPS. Figure 4h−i shows the XPS spectra of the Ir 4f and Mo 3d core-level shifts of a pristine, as-deposited IrMo sample (exposed to the atmosphere for a short period during the transport to the XPS facility), and an IrMo sample after 2 h of chronopotentiometry at 10 mA·cm^{-2}. Table S2 contains the fitting parameters used to deconvolute the XPS spectra. The Ir 4f core-level XPS spectrum of the as-deposited sample in Figure 4h suggests that Ir is initially primarily in the metallic state with a small amount of Ir^{4+} present. The 4+ oxidation state presumably develops on the film's surface during exposure to atmospheric air. The data in Figure 4h also show that after the conditioning and electrochemical testing, a large fraction of Ir atoms changes from the metallic to the oxidized state, indicating that there is a significant oxidation of the sample under reaction conditions. The Mo 3d spectrum in Figure 4i of IrMo before electrochemical testing shows intense peaks at 227.4 and 230.7 eV, which are indicative of metallic Mo, and also peaks at 227.9 and 231.7 eV, which are indicative of Mo^{4+}, as well as peaks at 228.7 and 233.8 eV, which are indicative of Mo^{5+}. Like the Ir 4f signal, the post-testing Mo 3d spectrum suggests that a large fraction of Mo atoms are oxidized under OER reaction conditions. The XPS spectra and cross-sectional TEM images for the monometallic Ir control samples are shown in Figures S6 and S12.

Computational Characterization of $Ir_{0.5}Mo_{0.5}O_x$ Stability and Activity. While, as described above, the IrMo thin-film electrocatalysts showed stable OER performance for the extended time, the ICP and electron microscopy measurements showed that there was some degradation of the alloy material. To analyze the potential pathways for the observed degradation, we performed additional computational characterization to gain further insight into the electrochemical stability and activity of the IrMo catalysts. In these studies, we computed a Pourbaix diagram of the Ir−Mo bond using a more computationally expensive SCAN functional. The SCAN functional has been argued to show some improvements in the agreement between computational Pourbaix diagrams and experimental data.[41] The computed Pourbaix diagram is shown in Figure 5a with the data used to construct the diagram reported in Table S3. The SCAN Pourbaix diagram suggests that neither $Ir_{0.5}Mo_{0.5}O_2$ nor $Ir_{0.5}Mo_{0.5}O_3$ are the most thermodynamically stable phases at any OER-relevant operating conditions.

Since the Pourbaix diagram shows only the thermodynamically most stable phases, we cannot rule out potential metastability based on the diagram data. We used the SCAN functional to evaluate the Pourbaix decomposition free energies of the mixed $Ir_{0.5}Mo_{0.5}O_x$ phases (Figure 5b) as a function of applied potential and at a fixed pH of 1. The data show that between 0.0 and 0.75 V vs SHE, the metallic mixed IrMo is thermodynamically the most stable phase. At higher potentials, as the oxidation starts taking place, the segregated IrO_2 and MoO_x phases are thermodynamically stable. It is important to realize that these segregated oxide phases are not substantially more stable than the mixed oxide phases. For example, the data show that between 0.75 and 1.25 V vs SHE, the metastable mixed $Ir_{0.5}Mo_{0.5}O_2$ phase is between 0.01 and 0.12 eV/atom less stable compared to the most stable segregated iridium oxide and molybdenum oxide phases, suggesting that it is reasonable to assume that this mixed oxide phase can be kinetically trapped. The data show that at more oxidizing potentials, $Ir_{0.5}Mo_{0.5}O_3$ becomes more stable than $Ir_{0.5}Mo_{0.5}O_2$. At very high oxidizing potentials (>1.75 V vs SHE), leaching of IrO_4^+ into the solution becomes thermodynamically preferred. Ultimately, the data suggest a relatively low thermodynamic driving force toward the decomposition of the mixed $Ir_{0.5}Mo_{0.5}O_3$ phase (structure IX in Figure 5c) at OER-relevant potentials (>1.23 V vs SHE) and pH = 1.

Since we use the fabrication strategy that initially results in mixed oxide materials, it is useful to explore how this approach might affect the persistence of the mixed oxide phases under experimental conditions. Work from Sun et al. proposes the concept of remnant metastability, which suggests that observable metastable crystalline phases are generally remnants of thermodynamic conditions, where they were once the lowest free-energy phase and that kinetic limitations are likely to inhibit phase transformation.[42] Although no $Ir_{0.5}Mo_{0.5}O_x$ polymorph is on the convex hull in the SCAN Pourbaix diagram, the IrMo phase is predicted as stable at reducing potentials, and this is the phase that we initially synthesized. The concept of remnant metastability suggests that the preferential stabilization of a mixed $Ir_{0.5}Mo_{0.5}O_x$ material rather than separate IrO_2 and MoO_2 or MoO_3 phases is plausible.

We note that the phases predicted to be stable for $Ir_{0.5}Mo_{0.5}O_x$ at pH = 1 from Bayesian optimization are shown in Figure 5c. Both $Ir_{0.5}Mo_{0.5}O_2$ and $Ir_{0.5}Mo_{0.5}O_3$ structures exhibit fully octahedral local coordination environments, which is generally found to be the most common coordination environment for both Ir- and Mo-containing structures.[43]

Since the IrMo material showed higher activity than Ir oxide toward the OER, we used DFT to calculate theoretical overpotentials on various $Ir_{0.5}Mo_{0.5}O_2$ and $Ir_{0.5}Mo_{0.5}O_3$ surfaces. Several prior studies have investigated the OER mechanism on Ir oxides in acid. While there have been some proposals involving the participation of lattice oxygen,[45−47] recent experiments that used online electrochemical mass spectrometry to monitor the OER on isotopically labeled IrO_2 in acid suggested that oxygen formation via the participation of lattice oxygen accounts for several orders of magnitude less oxygen formation than oxygen formation via an adsorbate evolution mechanism.[48] Therefore, we considered the adsorbate evolution OER mechanism that consists of four consecutive proton and electron transfer steps and proceeds through the *OH, *O, and *OOH adsorbates.[49,50] We studied the (001), (110), (013), and (103) surfaces for $Ir_{0.5}Mo_{0.5}O_2$ and the (002), (220), and (420) surfaces for $Ir_{0.5}Mo_{0.5}O_3$.

https://doi.org/10.1021/jacs.3c13491
J. Am. Chem. Soc. 2024, 146, 5511−5522

These surfaces were selected as their Miller indices exhibited the highest intensity diffraction peaks in simulated X-ray diffraction patterns (Figure S13). For all surfaces, we considered Ir metal centers octahedrally coordinated by O to be the active site. We selected this active site model based on the low predicted activity of MoO_2 and the fact that Ir atoms octahedrally coordinated by O are a well-known structural motif for Ir-based OER electrocatalysis.[51] Additional details regarding our calculation methodology are given in the Methods section. We give all computed reaction free energies in Table S4. In the adsorbate evolution mechanism, it is argued that the overpotential is governed by the adsorption free energy difference between *O and *OH on the active site, and therefore, it can be approximated by computing the difference in these absorption energies.[44] We computed these differences, and the results of these calculations are summarized in Figure 5d.

The data in Figure 5d suggest that both the $Ir_{0.5}Mo_{0.5}O_2$ and $Ir_{0.5}Mo_{0.5}O_3$ surfaces should exhibit competitive activities with their pure IrO_x counterparts. The activity improvements may result from the electronic modification of surface O species, such that they have higher-in-energy 2p states (Figures S14 and S15), which prior work has shown to correlate with the adsorption free energy difference between *O and *OH.[52] We also calculated theoretical overpotentials for a proposed mechanism that includes the participation of lattice oxygen on select surfaces of $Ir_{0.5}Mo_{0.5}O_2$ and $Ir_{0.5}Mo_{0.5}O_3$ and compared them to IrO_2 and IrO_3, with results shown in Figure S16. We found that the overpotential decreases moderately for $Ir_{0.5}Mo_{0.5}O_x$ materials compared to IrO_x materials for the lattice oxygen mechanism.[45,46]

In summary, the computational characterization presented in Figure 5 corroborates our experimental characterization, showing that IrMo is a promising catalyst for the OER in acidic media. Our Pourbaix analysis predicted that $Ir_{0.5}Mo_{0.5}O_3$ should have a low thermodynamic driving force toward decomposition at OER-relevant conditions, with plausible remnant metastability due to IrMo being a thermodynamically stable phase at low applied potentials, rationalizing the competitive stability observed experimentally. We also show that several $Ir_{0.5}Mo_{0.5}O_x$ model surfaces exhibit activities that are at least comparable to, and in many cases superior to, their pure IrO_x counterparts, rationalizing our improved experimentally observed activities.

■ CONCLUSIONS

In this work, we used BO to significantly accelerate a computational screening of the transition metal series for $Ir_{0.5}M_{0.5}O_x$ structural motifs that are stable under the corrosive oxidative potentials and low pHs present during the OER in acidic media. After our computational screening identified $Ir_{0.5}Mo_{0.5}O_x$ motifs as a potentially stable OER catalyst, we synthesized $Ir_{0.5}Mo_{0.5}O_x$ thin films on p^+-Si substrates, which demonstrated overpotentials 32 ± 3 mV lower than a pure IrO_x control when tested in acidic conditions. Experimental characterization of IrMo samples via ICP-MS, STEM, EDX, XPS, and steady-state electrochemical measurements revealed a 24% reduction in Ir leaching compared to a pure Ir sample and that IrMo samples can withstand the OER reaction conditions with minimal changes to surface topography and no reduction in onset potential. Importantly, Mo remains mixed well with Ir throughout testing. These results also provide evidence for the robustness and accuracy of our current theoretical understanding of the OER catalysts and provide a path for DFT- and ML-aided catalyst discovery.

■ METHODS

Bulk DFT Modeling of dDoped Ir Oxide Materials. The Vienna Ab initio Simulation Package (VASP) was used to perform all Kohn−Sham DFT calculations of $Ir_{0.5}M_{0.5}O_x$ materials.[53−56] Calculation settings were selected to be consistent with the total energy calculation methodology in the Materials Project.[57] Electron−ion interactions were described by the projector augmented wave method with a plane-wave kinetic-energy cutoff of 520 eV. Spin polarization was used for all calculations, with magnetic ions initiated in high-spin ferromagnetic states (i.e., MAGMOM = 5). Brillouin zone integration used a k-point mesh containing a total number of k-points equivalent to 64 times the volume of the reciprocal lattice (distributed proportionately along each lattice vector inversely proportional to their length) for all computations. The k-points were selected using the Monkhorst−Pack method and were Γ-centered for hexagonal cells.[58] Blochl's tetrahedron method was used for k-point integration.[57] Hubbard U corrections were used for $Ir_{0.5}M_{0.5}O_x$, in which M = V, Cr, Mn, Fe, Co, Ni, Mo, W, with the U values given by the Materials Project.[26,59] Electron exchange and correlation were approximated by the Perdew−Burke−Ernzerhof functional during the stability screening process[60,61] and by the meta-GGA SCAN functional when constructing the SCAN Pourbaix diagram.[62]

Our geometry relaxation strategy was informed by the work of Flores et al.[17] We first performed a relaxation of the unit cell shape and volume with fixed atom positions (ISIF = 6) to account for the initial geometries that were far from convergence. We next performed four relaxations in which all degrees of freedom, including atom positions, cell shape, and cell volume, were relaxed (ISIF = 3). We performed multiple relaxations to minimize the well-known basis errors associated with changing the unit cell size. Finally, we performed a single-point calculation to obtain the final electronic energy. All structures studied are available on the NOMAD repository at DOI: 10.17172/NOMAD/2024.01.25-1.

Bayesian Optimization Workflow. We used Gaussian process (GP) regression as the surrogate model in our Bayesian optimization workflow. The kernel used was a linear combination of radial basis function kernels

$$k(x, x') = s_1 \exp\left(-\frac{|x - x|'^{2}}{2l_1^2}\right) + s_2 \exp\left(-\frac{|x - x|'^{2}}{2l_2^2}\right) + \delta_{x,x'}$$

where l_i^2 is an anisotropic length factor that determines how far the GP model can extrapolate from the training data. We initialized $s_1 = l_1 = 1$ and $s_2 = l_2 = 0.5$, but ultimately, these parameters are learned from the training data. We selected this kernel because a similar kernel was previously used to describe both long- and short-range feature similarities in metal oxides and showed promising predictive performance.[17]

GP models were built using Scikit-learn[63] and learned using a Voronoi tessellation-based fingerprinting routine.[64] This fingerprinting scheme produced a feature vector containing 271 features that encoded both geometric and chemical information on the $Ir_{0.5}M_{0.5}O_x$ structures. We removed features with zero variance and then performed dimensionality reduction using principal component analysis to compress the data set to three features.[65] Three principal component features retained more than 99% of the variance in the original 271-length feature set (Figure S17), suggesting that a significant fraction of the original features contain redundant information, likely due to the fixed compositions and recurrent structural motifs present in the $Ir_{0.5}M_{0.5}O_x$ material data. The three principal component features are not interpretable because they are a linear combination of all of the remaining features. However, dimensionality reduction via principal component analysis led to speed improvements in the performance of the BO routine by reducing the dimensionality of the optimization space by nearly 2 orders of magnitude. In Figure 1, UMAP was applied to the original 271-length fingerprint.

We evaluated several acquisition functions (Figure S1) but ultimately opted to proceed with the acquisition function from the efficient global optimization algorithm,[23] which balances between exploration and exploitation by evaluating the expected improvement (EI) acquisition function and choosing the candidates with the largest EI. The EI was calculated as follows

$$\nu_{\mathrm{EI}} = (\bar{y}^*_{\min} - \mu)\Phi((\bar{y}^*_{\min} - \mu)/s) + s\phi((\bar{y}^*_{\min} - \mu)/s)$$

where $\bar{y}^*_{\min}$ is the minimum energy value in the training data, μ and s are the mean energy value and standard deviation from the GP model predicted energy value, and $\Phi(\cdot)$ and $\phi(\cdot)$ are the normal probability density and cumulative distribution functions, respectively.

Bayesian optimization workflows were initialized by selecting five $Ir_{0.5}M_{0.5}O_x$ polymorphs randomly and performing DFT-based geometry optimizations. These five polymorphs were used to train a GP model, which then selected the polymorph with the largest EI. The geometry of this polymorph was optimized by DFT, and then, the GP model was retrained with this polymorph added to the training set. This process was performed iteratively until at least 50 materials were studied and the EI was <1% of the lowest energy structure identified, which is a convergence (stopping) criterion that has been used previously.[23] Empirical testing of our BO workflows in Figure S1 shows that this convergence criterion is more than sufficient, considering that the lowest energy structure is typically found in ∼40 iterations. Example BO scripts are made available on GitHub at https://github.com/jesterhui/bayesian_optimization_iridium_molybdenum_oxide/tree/main.

Pourbaix Diagram Construction. We constructed Pourbaix diagrams using the Pourbaix diagram module implemented in the Pymatgen library.[27,29−31] This module identifies the Pourbaix stable domains by enumerating and comparing all potential combinations of compounds that satisfy a prespecified compositional constraint (e.g., Ir/Mo = 1:1) when in thermodynamic equilibrium with water. The equilibrium redox reaction can be expressed as

$$[\text{reactants}] + H_2O \Leftrightarrow [\text{products}] + mH^+ + ne^-$$

At equilibrium, the Nernst equation can be used to modify the reaction free energy (ΔrG) for all of these potential combinations of compounds as a function of applied potential (E) and pH using the following equation

$$-nFE = \Delta_r G = \Delta_r G^\circ + 2.303 \cdot RT \cdot \log\left(\frac{a_P}{a_R}\right) - 2.303 \cdot m \cdot RT \cdot \mathrm{pH}$$

where T is the temperature, F is the Faraday constant, R is the ideal gas constant, n is the number of electrons, m is the number of protons, a_i is an activity coefficient (where i = {R, P} denotes reactants and products, respectively), and pH is $-\log(a_{H^+})$. Identifying the species that minimize the difference between the contributions from the cell potential and the reaction Gibbs free energy (i.e., $\Delta_r G + nFE$) over the potential and pH values of interest then yields the Pourbaix diagram.

During the screening process, the chemical potentials of the reference solids were obtained from the Materials Project database.[26] We expressed the chemical potentials of the materials in the SCAN Pourbaix diagram in Figure 5 under standard conditions, μ^0, in the same manner as Wang et al.[41] Specifically, we used the equation

$$\mu^0 = H^\circ - TS^\circ = E_{\mathrm{DFT}} + E_{\mathrm{ZPE}} + \delta H - TS^\circ$$

where E_{DFT} is the DFT-calculated total energy, E_{ZPE} is the zero-point energy, δH is the integrated heat capacity (integrated from 0 to 298.15 K), and $TS°$ is the entropic contribution at standard conditions. For gas-phase O and H, the elemental references, respectively, corresponding to entries mp-1087546 and mp-1181189 in the Materials Project were used.[26] Gas-phase entropies for O and H were collected from the NIST-JANAF experimental thermodynamic tables.[66] Entropic contributions for solid-state materials were neglected because of their small size compared with gas-phase entropies. Energetic contributions from E_{ZPE} were omitted for both solid- and gas-phase species due to the assumption that different species have similar energetic contributions that largely cancel out in reaction energies, and δH was neglected because δH is typically less than 0.03 eV/atom.[67,68]

In constructing the SCAN-based Pourbaix diagrams, the chemical potentials of aqueous species, μ^0_{ion}, were obtained by correcting experimental values, $\mu^0_{\mathrm{ion,exp}}$, in a methodology consistent with what is used by the Materials Project.[26] Specifically, the experimental data were corrected using a solid−solid correction, $\Delta\mu_{\mathrm{solid-solid}}$. The correction was calculated as the energy difference between the experimental chemical potential and the DFT-calculated chemical potential of the reference solid.

$$\mu^0_{\mathrm{ion}} = \mu^0_{\mathrm{ion,exp}} + \Delta\mu_{\mathrm{solid-solid}}$$

The rationale behind this correction is that using a chemical potential for an aqueous ion that reproduces the correct dissolution energy for one solid ensures that other solids also dissolve accurately with respect to that ion's chemical potential. We used Ir (mp-101) and MoO_3 (mp-18856) as the reference solids. Experimental reference aqueous ion energies were taken from Pourbaix,[13] and experimental reference solid energies were taken from Barin and Platzki.[69−7071]

Evaluating OER Activities with Surface Thermodynamics. We created model surfaces of $Ir_{0.5}Mo_{0.5}O_2$ and $Ir_{0.5}Mo_{0.5}O_3$ by cleaving flat oxygen-terminated surfaces along the Miller indices with the highest intensity diffraction peaks based on simulated X-ray patterns (Figure S13). Slabs were constructed to be at least 10 Å thick in the z-direction, with at least 15 Å vacuum separating the surface from the slab's periodic image. Similar to the bulk calculations, VASP was used to perform all surface calculations.[53−56] We used the PBE functional to describe electron exchange and correlation,[60,61] and the projector augmented wave method to describe electron−ion interactions. A plane-wave kinetic-energy cutoff of 400 eV was selected, and a 6 × 6 × 1 Monkhorst−Pack k-point grid was used for the Brillouin zone integration.[58]

For all surfaces, the topmost surface layer of metal atoms in a slab and all of their coordinated oxygen atoms were optimized by conjugate gradient geometry optimization, while the remainder of the slab was fixed at the bulk lattice constant. Geometry optimizations were stopped once the maximum forces on all atoms in each system were less than 0.03 eV/Å. Collinear spin polarization was used for all surfaces. Hubbard U corrections were used for Mo species in $Ir_{0.5}Mo_{0.5}O_x$ with a U value of 4.38 eV from the Materials Project.[26,59] We calculated reaction free energies using H_2O and O_2 references corresponding to Materials Project entries mp-697111 and mp-12957, respectively. Zero-point energies and entropic contributions for all species were obtained from a previous study.[72] The H_2 reference was selected to reproduce the experimentally measured formation free energy of water at standard conditions, which is 2.46 eV/H_2O.[66] Solvent effects were neglected in the present work, but we note that prior work showed that the energetics of the OER reaction pathway remained relatively unchanged with the inclusion of explicit solvent.[73]

Preparation of IrO_x and $Ir_{0.5}Mo_{0.5}O_x$ Thin Films. Boron-doped (p-type, resistivity 0.001−0.005 $\Omega \cdot cm^{-1}$, (100)-oriented, 525 μm thick) Si wafers purchased from Addison Engineering were used as substrates for catalyst (either Ir or IrMo) deposition. Wafers were cleaned in Nanostrip, a commercial piranha solution, for 15 min. Native silicon oxide was removed by placing the wafers in a solution of buffered hydrofluoric acid for 2 min. The samples were then dried and placed under vacuum.

Thin films of the catalyst were deposited on the Si substrate using a loadlocked magnetron sputter tool from Kurt J. Lesker Company. The IrMo catalyst was created through codepositing Ir and Mo with the following recipe: An Ir shutter source was deposited at 150 W at a rate of 1.23 $Å \cdot s^{-1}$, and Mo was deposited at 173 W at a rate of 1.23 $Å \cdot s^{-1}$. For the Ir control, 10 nm of Ir was deposited at 100 W at a rate of 1.19 $Å \cdot s^{-1}$. The catalyst wafers were then hand-diced into 12 mm ×

12 mm samples using a diamond scribe and LatticeGear clean break pliers.

Material Characterization. Cross-sectional STEM samples were prepared using focused ion-beam milling on a Thermo Fisher Nova 200 Nanolab. STEM images and EDS spectra were obtained on a Thermo Fisher Talos F200X G2 using a double tilt holder. All samples were aligned to the silicon crystal lattice to ensure a perpendicular view of the cross section. XPS spectra were obtained using a Kratos Axis Ultra XPS with an emission current of 10 mA and a voltage of 12 mV. The C 1s peaks were aligned to 284.8 eV, and CasaXPS software was used for all peak fittings.

Inductively coupled plasma mass spectroscopy (ICP-MS) was used to obtain trace metal content of Ir and Mo in solution at different stages of testing. Electrolyte solutions were processed using a PerkinElmer Nexion 2000 ICP-MS. We made 5 mL calibration curves using ICP-grade stock solutions from Ricca Chemicals (Ir) and SPEX CertiPrep (Mo). ICP-MS was calibrated using a Bismuth internal standard, and the resulting calibration curves had an r^2 value of greater than 0.99.

Electrochemical Measurements. The 12 mm × 12 mm catalyst samples were housed in a 3D printed electrode with an aperture area of 0.4591 cm^2, which ensured that a constant area was exposed to the electrolyte across samples. The backs of the samples were scratched with a diamond scribe, and a small amount of indium−gallium eutectic paint (99.99%) was adhered to the scratched area to ensure an Ohmic contact. The back contact was placed against a copper plate. A solution of 0.1 M perchloric acid was prepared for electrochemical testing using 70 wt % perchloric acid (Sigma-Aldrich, 99.999% trace metals basis) with a pH of 1. The reference electrode was a silver/silver chloride electrode (Ag/AgCl, Pine, FODR-0021), and the counter electrode was a Pt wire. The reference electrode was calibrated to the reversible hydrogen electrode (RHE) in a H_2-saturated electrolyte.

We used a standardized electrochemical procedure across all samples. First, the samples were swept by using cyclic voltammetry to obtain their overpotentials. The samples were then held at a low current of 1 $mA \cdot cm^{-2}$ using chronopotentiometry to convert the Ir bulk metal to an Ir oxide phase for higher stability. Additional details can be found in Supplementary Note 2 and Figures S6 and S7, which gives the XPS spectra of Ir and IrMo after oxidative conditioning. Cyclic voltammetry was performed again, and then, steady-state measurements at 10 $mA \cdot cm^{-2}$ were gathered for two hours in intervals of 5, 15, 30, 60, and 120 min. CV measurements were obtained after steady-state testing, and resistance measurements were taken using electrochemical impedance spectroscopy after preliminary testing, oxidative conditioning, and steady-state testing. All CV measurements presented have been *iR*-corrected using solution resistance gathered from EIS measurements.

ASSOCIATED CONTENT

Supporting Information

The Supporting Information is available free of charge at https://pubs.acs.org/doi/10.1021/jacs.3c13491.

> Evaluation of acquisition functions for Bayesian optimization; progress of Bayesian optimization workflow for $Ir_{0.5}Mo_{0.5}O_3$ and calibration curves; XPS spectra and ICP-MS data of IrMo samples and Ir control; TEM micrographs of IrMo and Ir samples; tables of free energies of formation; simulated XRD patterns; d-projected DOS for Ir-based systems; reaction free energy diagrams for different OER mechanisms; variance explained by principal components of the fingerprinted $Ir_{0.5}Mo_{0.5}O_x$ data sets (PDF)

AUTHOR INFORMATION

Corresponding Author

[‖]Suljo Linic − *Department of Chemical Engineering, University of Michigan, Ann Arbor, Michigan 48109-2136, United States; Catalysis Science and Technology Institute, University of Michigan, Ann Arbor, Michigan 48109-2136, United States;* orcid.org/0000-0003-2153-6755; Email: linic@umich.edu

Authors

Jacques A. Esterhuizen − *Department of Chemical Engineering, University of Michigan, Ann Arbor, Michigan 48109-2136, United States; Catalysis Science and Technology Institute, University of Michigan, Ann Arbor, Michigan 48109-2136, United States;* orcid.org/0000-0002-2582-3172

Aarti Mathur − *Department of Chemical Engineering, University of Michigan, Ann Arbor, Michigan 48109-2136, United States; Catalysis Science and Technology Institute, University of Michigan, Ann Arbor, Michigan 48109-2136, United States*

Bryan R. Goldsmith − *Department of Chemical Engineering, University of Michigan, Ann Arbor, Michigan 48109-2136, United States; Catalysis Science and Technology Institute, University of Michigan, Ann Arbor, Michigan 48109-2136, United States;* orcid.org/0000-0003-1264-8018

Complete contact information is available at: https://pubs.acs.org/10.1021/jacs.3c13491

Author Contributions

[§]J.A.E. and A.M. contributed equally to the work.

Notes

The authors declare no competing financial interest.

[‖]S.L. is lead contact.

ACKNOWLEDGMENTS

The authors acknowledge support from the US Department of Energy Office of Basic Energy Sciences, Division of Chemical Sciences (DE-SC0021362). They also acknowledge support from the National Science Foundation under Grant No. (CBET-2116646) for supporting the computational efforts. This research used the National Energy Research Scientific Computing Center resources, a U.S. Department of Energy Office of Science User Facility, operated under Contract No. DE-AC02-05CH11231. The authors acknowledge the Michigan Center for Materials Characterization for subsidizing the use of characterization instruments through National Science Foundation grants #DMR-0320740 and #DMR-0420785. J.A.E. acknowledges support from the University of Michigan J. Robert Beyster Computational Innovation Graduate Fellows Program. A.M acknowledges support from the Department of Defense through the National Defense Science & Engineering Graduate Fellowship Program.

REFERENCES

(1) Ursua, A.; Gandia, L. M.; Sanchis, P. Hydrogen Production From Water Electrolysis: Current Status and Future Trends. *Proc. IEEE* **2012**, *100* (2), 410−426.

(2) Reier, T.; Nong, H. N.; Teschner, D.; Schlögl, R.; Strasser, P. Electrocatalytic Oxygen Evolution Reaction in Acidic Environments − Reaction Mechanisms and Catalysts. *Adv. Energy Mater.* **2017**, *7* (1), No. 1601275.

(3) Katsounaros, I.; Cherevko, S.; Zeradjanin, A. R.; Mayrhofer, K. J. J. Oxygen Electrochemistry as a Cornerstone for Sustainable Energy Conversion. *Angew. Chem., Int. Ed.* **2014**, *53* (1), 102−121.

(4) Fabbri, E.; Habereder, A.; Waltar, K.; Kötz, R.; Schmidt, T. J. Developments and Perspectives of Oxide-Based Catalysts for the Oxygen Evolution Reaction. *Catal. Sci. Technol.* **2014**, *4* (11), 3800−3821.

(5) McCrory, C. C. L.; Jung, S.; Peters, J. C.; Jaramillo, T. F. Benchmarking Heterogeneous Electrocatalysts for the Oxygen Evolution Reaction. *J. Am. Chem. Soc.* **2013**, *135* (45), 16977−16987.

(6) McCrory, C. C. L.; Jung, S.; Ferrer, I. M.; Chatman, S. M.; Peters, J. C.; Jaramillo, T. F. Benchmarking Hydrogen Evolving Reaction and Oxygen Evolving Reaction Electrocatalysts for Solar Water Splitting Devices. *J. Am. Chem. Soc.* **2015**, *137* (13), 4347−4357.

(7) Strickler, A. L.; Flores, R. A.; King, L. A.; Nørskov, J. K.; Bajdich, M.; Jaramillo, T. F. Systematic Investigation of Iridium-Based Bimetallic Thin Film Catalysts for the Oxygen Evolution Reaction in Acidic Media. *ACS Appl. Mater. Interfaces* **2019**, *11* (37), 34059−34066.

(8) Seitz, L. C.; Dickens, C. F.; Nishio, K.; Hikita, Y.; Montoya, J.; Doyle, A.; Kirk, C.; Vojvodic, A.; Hwang, H. Y.; Norskov, J. K.; Jaramillo, T. F. A Highly Active and Stable IrOx/SrIrO3 Catalyst for the Oxygen Evolution Reaction. *Science* **2016**, *353*, 1011−1014.

(9) Hubert, M. A.; Patel, A. M.; Gallo, A.; Liu, Y.; Valle, E.; Ben-Naim, M.; Sanchez, J.; Sokaras, D.; Sinclair, R.; Nørskov, J. K.; King, L. A.; Bajdich, M.; Jaramillo, T. F. Acidic Oxygen Evolution Reaction Activity−Stability Relationships in Ru-Based Pyrochlores. *ACS Catal.* **2020**, *10* (20), 12182−12196.

(10) Hubert, M. A.; Gallo, A.; Liu, Y.; Valle, E.; Sanchez, J.; Sokaras, D.; Sinclair, R.; King, L. A.; Jaramillo, T. F. Characterization of a Dynamic Y2Ir2O7 Catalyst during the Oxygen Evolution Reaction in Acid. *J. Phys. Chem. C* **2022**, *126* (4), 1751−1760.

(11) Buvat, G.; Eslamibidgoli, M. J.; Garbarino, S.; Eikerling, M.; Guay, D. OER Performances of Cationic Substituted (100)-Oriented IrO2 Thin Films: A Joint Experimental and Theoretical Study. *ACS Appl. Energy Mater.* **2020**, *3* (6), 5229−5237.

(12) Shi, X.; Peng, H.-J.; Hersbach, T. J. P.; Jiang, Y.; Zeng, Y.; Baek, J.; Winther, K. T.; Sokaras, D.; Zheng, X.; Bajdich, M. Efficient and Stable Acidic Water Oxidation Enabled by Low-Concentration, High-Valence Iridium Sites. *ACS Energy Lett.* **2022**, *7*, 2228−2235.

(13) Pourbaix, M. *Atlas of Electrochemical Equilibria in Aqueous Solutions*, 1st ed.; Pergamon Press: Oxford, 1966.

(14) Wan, G.; Freeland, J. W.; Kloppenburg, J.; Petretto, G.; Nelson, J. N.; Kuo, D.-Y.; Sun, C.-J.; Wen, J.; Diulus, J. T.; Herman, G. S.; Dong, Y.; Kou, R.; Sun, J.; Chen, S.; Shen, K. M.; Schlom, D. G.; Rignanese, G.-M.; Hautier, G.; Fong, D. D.; Feng, Z.; Zhou, H.; Suntivich, J. Amorphization Mechanism of SrIrO3 Electrocatalyst: How Oxygen Redox Initiates Ionic Diffusion and Structural Reorganization. *Sci. Adv.* **2021**, *7* (2), No. eabc7323.

(15) Grimaud, A.; Demortière, A.; Saubanère, M.; Dachraoui, W.; Duchamp, M.; Doublet, M.-L.; Tarascon, J.-M. Activation of Surface Oxygen Sites on an Iridium-Based Model Catalyst for the Oxygen Evolution Reaction. *Nat. Energy* **2017**, *2* (1), 1−10.

(16) Rao, K. K.; Lai, Y.; Zhou, L.; Haber, J. A.; Bajdich, M.; Gregoire, J. M. Overcoming Hurdles in Oxygen Evolution Catalyst Discovery via Codesign. *Chem. Mater.* **2022**, *34* (3), 899−910.

(17) Flores, R. A.; Paolucci, C.; Winther, K. T.; Jain, A.; Torres, J. A. G.; Aykol, M.; Montoya, J.; Nørskov, J. K.; Bajdich, M.; Bligaard, T. Active Learning Accelerated Discovery of Stable Iridium Oxide Polymorphs for the Oxygen Evolution Reaction. *Chem. Mater.* **2020**, *32* (13), 5854−5863.

(18) Graff, D. E.; I Shakhnovich, E.; W Coley, C. Accelerating High-Throughput Virtual Screening through Molecular Pool-Based Active Learning. *Chem. Sci.* **2021**, *12* (22), 7866−7881.

(19) Deshwal, A.; Simon, C. M.; Doppa, J. R. Bayesian Optimization of Nanoporous Materials. *Mol. Syst. Des. Eng.* **2021**, *6* (12), 1066−1086.

(20) Janet, J. P.; Ramesh, S.; Duan, C.; Kulik, H. J. Accurate Multiobjective Design in a Space of Millions of Transition Metal Complexes with Neural-Network-Driven Efficient Global Optimization. *ACS Cent. Sci.* **2020**, *6* (4), 513−524.

(21) Pedersen, J. K.; Clausen, C. M.; Krysiak, O. A.; Xiao, B.; Batchelor, T. A. A.; Löffler, T.; Mints, V. A.; Banko, L.; Arenz, M.; Savan, A.; Schuhmann, W.; Ludwig, A.; Rossmeisl, J. Bayesian Optimization of High-Entropy Alloy Compositions for Electrocatalytic Oxygen Reduction**. *Angew. Chem., Int. Ed.* **2021**, *60* (45), 24144−24152.

(22) Rasmussen, C. E.; Bousquet, O.; von Luxburg, U.; Rätsch, G. Gaussian Processes in Machine Learning. In *Advanced Lectures on Machine Learning: ML Summer Schools 2003, Canberra, Australia, February 2 - 14, 2003, Tübingen, Germany, August 4 - 16, 2003, Revised Lectures*, Lecture Notes in Computer Science; Springer: Berlin, Heidelberg, 2004; pp 63−71.

(23) Jones, D. R.; Schonlau, M.; Welch, W. J. Efficient Global Optimization of Expensive Black-Box Functions. *J. Glob. Optim.* **1998**, *13* (4), 455−492.

(24) Kushner, H. J. A New Method of Locating the Maximum Point of an Arbitrary Multipeak Curve in the Presence of Noise. *J. Basic Eng.* **1964**, *86* (1), 97−106.

(25) Cox, D. D.; John, S.SDO: A Statistical Method for Global Optimization *In Multidisciplinary Design Optimization: State-of-the-Art* 1997, pp 315−329.

(26) Jain, A.; Ong, S. P.; Hautier, G.; Chen, W.; Richards, W. D.; Dacek, S.; Cholia, S.; Gunter, D.; Skinner, D.; Ceder, G.; Persson, K. A. Commentary: The Materials Project: A Materials Genome Approach to Accelerating Materials Innovation. *APL Mater.* **2013**, *1* (1), No. 011002.

(27) Ong, S. P.; Richards, W. D.; Jain, A.; Hautier, G.; Kocher, M.; Cholia, S.; Gunter, D.; Chevrier, V. L.; Persson, K. A.; Ceder, G. Python Materials Genomics (Pymatgen): A Robust, Open-Source Python Library for Materials Analysis. *Comput. Mater. Sci.* **2013**, *68*, 314−319.

(28) McInnes, L.; Healy, J.; Melville, J. UMAP: Uniform Manifold Approximation and Projection for Dimension Reduction. 2018, arXiv:1802.03426. arXiv.org e-Print archive. https://arxiv.org/abs/1802.03426 (accessed Nov 30, 2023).

(29) Persson, K. A.; Waldwick, B.; Lazic, P.; Ceder, G. Prediction of Solid-Aqueous Equilibria: Scheme to Combine First-Principles Calculations of Solids with Experimental Aqueous States. *Phys. Rev. B* **2012**, *85* (23), No. 235438.

(30) Singh, A. K.; Zhou, L.; Shinde, A.; Suram, S. K.; Montoya, J. H.; Winston, D.; Gregoire, J. M.; Persson, K. A. Electrochemical Stability of Metastable Materials. *Chem. Mater.* **2017**, *29* (23), 10159−10167.

(31) Patel, A. M.; Nørskov, J. K.; Persson, K. A.; Montoya, J. H. Efficient Pourbaix Diagrams of Many-Element Compounds. *Phys. Chem. Chem. Phys.* **2019**, *21* (45), 25323−25327.

(32) Pan, H.; Ganose, A. M.; Horton, M.; Aykol, M.; Persson, K. A.; Zimmermann, N. E. R.; Jain, A. Benchmarking Coordination Number Prediction Algorithms on Inorganic Crystal Structures. *Inorg. Chem.* **2021**, *60* (3), 1590−1603.

(33) *Mineral Commodity Summaries 2022; Mineral Commodity Summaries; USGS Numbered Series 2022*; U.S. Geological Survey: Reston, VA, 2022.

(34) Zheng, Y.-R.; Vernieres, J.; Wang, Z.; Zhang, K.; Hochfilzer, D.; Krempl, K.; Liao, T.-W.; Presel, F.; Altantzis, T.; Fatermans, J.; Scott, S. B.; Secher, N. M.; Moon, C.; Liu, P.; Bals, S.; Van Aert, S.; Cao, A.; Anand, M.; Nørskov, J. K.; Kibsgaard, J.; Chorkendorff, I. Monitoring Oxygen Production on Mass-Selected Iridium−Tantalum Oxide Electrocatalysts. *Nat. Energy* **2022**, *7*, 55−64.

(35) Guo, H.; Fang, Z.; Li, H.; Fernandez, D.; Henkelman, G.; Humphrey, S. M.; Yu, G. Rational Design of Rhodium−Iridium Alloy Nanoparticles as Highly Active Catalysts for Acidic Oxygen Evolution. *ACS Nano* **2019**, *13* (11), 13225−13234.

(36) Lv, F.; Feng, J.; Wang, K.; Dou, Z.; Zhang, W.; Zhou, J.; Yang, C.; Luo, M.; Yang, Y.; Li, Y.; Gao, P.; Guo, S. Iridium−Tungsten

Alloy Nanodendrites as pH-Universal Water-Splitting Electrocatalysts. *ACS Cent. Sci.* **2018**, *4* (9), 1244−1252.

(37) Elmaalouf, M.; Odziomek, M.; Duran, S.; Gayrard, M.; Bahri, M.; Tard, C.; Zitolo, A.; Lassalle-Kaiser, B.; Piquemal, J.-Y.; Ersen, O.; Boissière, C.; Sanchez, C.; Giraud, M.; Faustini, M.; Peron, J. The Origin of the High Electrochemical Activity of Pseudo-Amorphous Iridium Oxides. *Nat. Commun.* **2021**, *12* (1), No. 3935.

(38) Tariq, M.; Zaman, W. Q.; Sun, W.; Zhou, Z.; Wu, Y.; Cao, L.; Yang, J. Unraveling the Beneficial Electrochemistry of IrO2/MoO3 Hybrid as a Highly Stable and Efficient Oxygen Evolution Reaction Catalyst. *ACS Sustainable Chem. Eng.* **2018**, *6* (4), 4854−4862.

(39) Ahn, S. H.; Jin, D.; Lee, C.; Lee, Y. Oxygen-Vacancy Rich IrxMo1−xOy Nanofibers for Oxygen Evolution Reaction: Excellent pH-Universal and Electrolyte-Concentration-Independent Catalytic Activity. *J. Mater. Chem. A* **2023**, *11* (27), 14941−14951.

(40) Chen, S.; Zhang, S.; Guo, L.; Pan, L.; Shi, C.; Zhang, X.; Huang, Z.-F.; Yang, G.; Zou, J.-J. Reconstructed Ir−O−Mo Species with Strong Brønsted Acidity for Acidic Water Oxidation. *Nat. Commun.* **2023**, *14* (1), No. 4127.

(41) Wang, Z.; Guo, X.; Montoya, J.; Nørskov, J. K. Predicting Aqueous Stability of Solid with Computed Pourbaix Diagram Using SCAN Functional. *npj Comput. Mater.* **2020**, *6* (1), No. 160.

(42) Sun, W.; Dacek, S. T.; Ong, S. P.; Hautier, G.; Jain, A.; Richards, W. D.; Gamst, A. C.; Persson, K. A.; Ceder, G. The Thermodynamic Scale of Inorganic Crystalline Metastability. *Sci. Adv.* **2016**, *2* (11), No. e1600225.

(43) Waroquiers, D.; Gonze, X.; Rignanese, G.-M.; Welker-Nieuwoudt, C.; Rosowski, F.; Göbel, M.; Schenk, S.; Degelmann, P.; André, R.; Glaum, R.; Hautier, G. Statistical Analysis of Coordination Environments in Oxides. *Chem. Mater.* **2017**, *29* (19), 8346−8360.

(44) Man, I. C.; Su, H.-Y.; Calle-Vallejo, F.; Hansen, H. A.; Martínez, J. I.; Inoglu, N. G.; Kitchin, J.; Jaramillo, T. F.; Nørskov, J. K.; Rossmeisl, J. Universality in Oxygen Evolution Electrocatalysis on Oxide Surfaces. *ChemCatChem* **2011**, *3* (7), 1159−1165.

(45) Zagalskaya, A.; Evazzade, I.; Alexandrov, V. Ab Initio Thermodynamics and Kinetics of the Lattice Oxygen Evolution Reaction in Iridium Oxides. *ACS Energy Lett.* **2021**, *6* (3), 1124−1133.

(46) Zagalskaya, A.; Alexandrov, V. Role of Defects in the Interplay between Adsorbate Evolving and Lattice Oxygen Mechanisms of the Oxygen Evolution Reaction in RuO $_2$ and IrO$_2$. *ACS Catal.* **2020**, *10* (6), 3650−3657.

(47) Binninger, T.; Mohamed, R.; Waltar, K.; Fabbri, E.; Levecque, P.; Kötz, R.; Schmidt, T. J. Thermodynamic Explanation of the Universal Correlation between Oxygen Evolution Activity and Corrosion of Oxide Catalysts. *Sci. Rep.* **2015**, *5* (1), No. 12167.

(48) Geiger, S.; Kasian, O.; Ledendecker, M.; Pizzutilo, E.; Mingers, A. M.; Fu, W. T.; Diaz-Morales, O.; Li, Z.; Oellers, T.; Fruchter, L.; Ludwig, A.; Mayrhofer, K. J. J.; Koper, M. T. M.; Cherevko, S. The Stability Number as a Metric for Electrocatalyst Stability Benchmarking. *Nat. Catal.* **2018**, *1* (7), 508−515.

(49) Rossmeisl, J.; Logadottir, A.; Nørskov, J. K. Electrolysis of Water on (Oxidized) Metal Surfaces. *Chem. Phys.* **2005**, *319* (1), 178−184.

(50) Rossmeisl, J.; Qu, Z.-W.; Zhu, H.; Kroes, G.-J.; Nørskov, J. K. Electrolysis of Water on Oxide Surfaces. *J. Electroanal. Chem.* **2007**, *607* (1), 83−89.

(51) Willinger, E.; Massué, C.; Schlögl, R.; Willinger, M. G. Identifying Key Structural Features of IrO $_x$ Water Splitting Catalysts. *J. Am. Chem. Soc.* **2017**, *139* (34), 12093−12101.

(52) Dickens, C. F.; Montoya, J. H.; Kulkarni, A. R.; Bajdich, M.; Nørskov, J. K. An Electronic Structure Descriptor for Oxygen Reactivity at Metal and Metal-Oxide Surfaces. *Surf. Sci.* **2019**, *681*, 122−129.

(53) Kresse, G.; Hafner, J. Ab Initio Molecular Dynamics for Liquid Metals. *Phys. Rev. B* **1993**, *47* (1), 558−561.

(54) Kresse, G.; Hafner, J. Ab Initio Molecular-Dynamics Simulation of the Liquid-Metal–Amorphous-Semiconductor Transition in Germanium. *Phys. Rev. B* **1994**, *49* (20), 14251−14269.

(55) Kresse, G.; Furthmüller, J. Efficiency of Ab-Initio Total Energy Calculations for Metals and Semiconductors Using a Plane-Wave Basis Set. *Comput. Mater. Sci.* **1996**, *6* (1), 15−50.

(56) Kresse, G.; Furthmüller, J. Efficient Iterative Schemes for Ab Initio Total-Energy Calculations Using a Plane-Wave Basis Set. *Phys. Rev. B* **1996**, *54* (16), 11169−11186.

(57) Blöchl, P. E.; Jepsen, O.; Andersen, O. K. Improved Tetrahedron Method for Brillouin-Zone Integrations. *Phys. Rev. B* **1994**, *49* (23), 16223−16233.

(58) Monkhorst, H. J.; Pack, J. D. Special Points for Brillouin-Zone Integrations. *Phys. Rev. B* **1976**, *13* (12), 5188−5192.

(59) Wang, L.; Maxisch, T.; Ceder, G. Oxidation Energies of Transition Metal Oxides within the GGA + U Framework. *Phys. Rev. B* **2006**, *73* (19), No. 195107.

(60) Perdew, J. P.; Burke, K.; Ernzerhof, M. Generalized Gradient Approximation Made Simple. *Phys. Rev. Lett.* **1996**, *77* (18), 3865−3868.

(61) Perdew, J. P.; Burke, K.; Ernzerhof, M. Generalized Gradient Approximation Made Simple [Phys. Rev. Lett. 77, 3865 (1996)]. *Phys. Rev. Lett.* **1997**, *78* (7), 1396.

(62) Sun, J.; Ruzsinszky, A.; Perdew, J. P. Strongly Constrained and Appropriately Normed Semilocal Density Functional. *Phys. Rev. Lett.* **2015**, *115* (3), No. 036402.

(63) Pedregosa, F.; Varoquaux, G.; Gramfort, A.; Michel, V.; Thirion, B.; Grisel, O.; Blondel, M.; Prettenhofer, P.; Weiss, R.; Dubourg, V.; Vanderplas, J.; Passos, A.; Cournapeau, D.; Brucher, M.; Perrot, M.; Duchesnay, E. Scikit-Learn: Machine Learning in Python. *J. Mach. Learn. Res.* **2011**, *12*, 2825−2830.

(64) Ward, L.; Liu, R.; Krishna, A.; Hegde, V. I.; Agrawal, A.; Choudhary, A.; Wolverton, C. Including Crystal Structure Attributes in Machine Learning Models of Formation Energies via Voronoi Tessellations. *Phys. Rev. B* **2017**, *96* (2), No. 024104.

(65) Hastie, T.; Friedman, J.; Tibshirani, R. *The Elements of Statistical Learning*; Hastie, T.; Friedman, J.; Tibshirani, R., Eds.; Springer Series in Statistics; Springer New York: New York, NY, 2001.

(66) Chase, M. W.; National Institute of Standards and Technology (U.S.). *NIST-JANAF Thermochemical Tables*; American Chemical Society; American Institute of Physics for the National Institute of Standards and Technology: Washington, D.C.; Woodbury, N.Y., 1998.

(67) Jain, A.; Hautier, G.; Ong, S. P.; Moore, C. J.; Fischer, C. C.; Persson, K. A.; Ceder, G. Formation Enthalpies by Mixing GGA and GGA + U Calculations. *Phys. Rev. B* **2011**, *84* (4), No. 045115, DOI: 10.1103/PhysRevB.84.045115.

(68) Lany, S. Semiconductor Thermochemistry in Density Functional Calculations. *Phys. Rev. B* **2008**, *78* (24), No. 245207.

(69) Barin, I.; Platzki, G. *Thermochemical Data of Pure Substances*; VCH: Weinheim; New York, 1995.

(70) Blöchl, P. E. Projector Augmented-Wave Method. *Phys. Rev. B* **1994**, *50* (24), 17953−17979.

(71) Kresse, G.; Joubert, D. From Ultrasoft Pseudopotentials to the Projector Augmented-Wave Method. *Phys. Rev. B* **1999**, *59* (3), 1758−1775.

(72) Montoya, J. H.; Doyle, A. D.; Nørskov, J. K.; Vojvodic, A. Trends in Adsorption of Electrocatalytic Water Splitting Intermediates on Cubic ABO3 Oxides. *Phys. Chem. Chem. Phys.* **2018**, *20* (5), 3813−3818.

(73) Gauthier, J. A.; Dickens, C. F.; Chen, L. D.; Doyle, A. D.; Nørskov, J. K. Solvation Effects for Oxygen Evolution Reaction Catalysis on IrO2(110). *J. Phys. Chem. C* **2017**, *121* (21), 11455−11463.